IOP Publishing Smart Materials and Structures
Smart Mater. Struct. **31** (2022) 095044 (12pp) https://doi.org/10.1088/1361-665X/ac858b

Duffing-type digitally programmable nonlinear synthetic inductance for piezoelectric structures

Obaidullah Alfahmi, Christopher Sugino and Alper Erturk*

G.W. Woodruff School of Mechanical Engineering, Georgia Institute of Technology, Atlanta, GA 30332, United States of America

E-mail: alper.erturk@me.gatech.edu

Received 22 May 2022, revised 22 July 2022
Accepted for publication 28 July 2022
Published 17 August 2022

Abstract

Piezoelectric shunt damping techniques using linear circuits (e.g. resistive-inductive) and switching circuits (e.g. synchronized switch on inductor) have been extremely well studied for suppressing resonant vibrations in flexible structures. Both analog circuits and synthetic impedance circuits with digital control have been explored for linear concepts. In a parallel body of work, from the domain of mechanical methods of vibration attenuation, it is also known that leveraging nonlinearities (e.g. stiffness nonlinearity) can enhance the frequency bandwidth and offer amplitude-dependent suppression over a range of frequencies. However, the existing piezoelectric shunt damping techniques have been mostly limited to linear or switching nonlinear circuits, with the exception of a few nonlinear capacitance efforts. This work aims to introduce cubic inductance to emulate Duffing-type hardening nonlinearity in the shunt circuit with precise digital programming and tuning capability. Experiments are performed on a piezoelectric bimorph cantilever under base excitation for concept demonstration and model validation. First, linear frequency response functions of the cantilever are obtained for the short- and open-circuit conditions, and for linear resistive-inductive synthetic shunt damping, to confirm the standard linear behavior and electromechanical model parameters. Then, cubic inductance is introduced to the circuit and nonlinear experiments (up- and down-frequency sweep) are conducted. Cantilever tip to base motion transmissibility frequency response is measured along with piezoelectric voltage to base motion counterpart for a range of base excitation amplitudes. The distortion of the frequency response curves with increased base acceleration levels is observed. The nonlinear cubic coefficient is then varied to alter the manifestation of nonlinear frequency response at a given base excitation level, demonstrating the ease of tuning and triggering the nonlinear behavior on demand by means of the digitally-controlled synthetic impedance shunt. Nonlinear electromechanical model simulations are also validated against the experiments, yielding a very good agreement.

Keywords: piezoelectricity, synthetic impedance, nonlinearity, shunt damping, vibration attenuation

(Some figures may appear in colour only in the online journal)

* Author to whom any correspondence should be addressed.

1. Introduction

The study of nonlinearity in dynamical systems has captivated researchers for decades not only for a fundamental understanding but also to leverage nonlinear dynamic phenomena in engineering problems. The broad range of examples span from vibration absorption [1, 2] and isolation [3, 4] to energy harvesting [5], where designed and intentionally introduced nonlinearities can be exploited for performance and bandwidth enhancement. In some cases, inherent material nonlinearities also need to be understood and accurately modeled [6, 7]. The focus of our present work is the domain of research that leverages nonlinearities in vibration absorption. Researchers have long explored the performance of a nonlinear mechanical oscillator attached to a linear primary system [8–10]. Introducing nonlinearities via monostable and bistable absorbers enhanced the vibration mitigation performance compared to their linear counterparts.

Since traditional mechanical vibration absorption methods cause considerable mass loading, which is not tolerable in a variety of applications (e.g. aerospace structures), piezoelectric shunt damping [11, 12] has been widely used in the field of vibration attenuation, especially for flexible and light-weight structures. Numerous works have explored different types of linear and nonlinear piezoelectric shunt damping techniques. Beyond the linear shunt circuits (such as standard resistive-inductive circuits [13]), state switched shunts [14, 15] and synchronized switching damping [16–19] have been proposed. Others have explored nonlinear inductive and capacitive circuit elements for vibration absorption [20, 21] (numerically or through analog circuit components). Essentially nonlinear piezoelectric shunt circuitry [22, 23] approaches were also investigated for the realization of a nonlinear energy sink for wideband absorption. Relying on nonlinear material (ferroelectric) capacitance [22] and analog circuits components [23] are relatively limited in terms of tunability, and analog circuits can often be cumbersome.

An easily tunable and programmable approach to electromechanical vibration absorption is the use of synthetic impedance circuits, which emulate the impedance of arbitrary electrical circuits by supplying current to the primary system in response to piezoelectric voltage (more as a synthetic admittance in that regard). The main advantage of applying synthetic impedance circuitry over analog piezoelectric shunt damping is the significantly greater flexibility and precision in realizing arbitrary shunt circuit elements and their tuning via digital signal processing. There have been several efforts leveraging linear synthetic impedance circuits. Fleming *et al* [24] proposed a simple synthetic impedance circuit for piezoelectric shunt damping applications. More recently, Matten *et al* [25] developed a digital synthetic impedance for shunting a piezoelectric element with experimental validation. Likewise, Nečásek *et al* [26] designed and tested a device capable of emulating different forms of electrical impedances. In most of the existing efforts, linear synthetic impedance circuits have been successfully applied for vibration suppression, with the exception of nonlinear capacitance in a recent work [27]. Our present work aims to focus on nonlinear (cubic) hardening inductance (of Duffing type) and its realization and programmability via synthetic impedance shunt.

In the following, we demonstrate a programmable nonlinear synthetic impedance circuit shunted to a linear primary structure. The focus is placed on digitally programmable nonlinear circuit emulation capability rather than designing and optimizing a vibration absorber. Specifically, we demonstrate a strongly nonlinear Duffing-type inductance with hardening cubic nonlinearity and the tunability of the nonlinear coefficient. In section 2, a brief overview of the synthetic impedance circuit is given. The derivation of the governing equations of the system is discussed in section 3, starting from linear shunts with resistive and resistive-inductive circuits (for linear parameter validation) and extending to the nonlinear shunt by introducing a cubic inductor to the linear resistive-inductive shunt. The system response is modeled for time-domain numerical simulations to predict the experimental frequency response functions (FRFs) of vibration transmissibility and voltage output. Section 4 presents experimental demonstration of the hardening Duffing circuit and validation of the electromechanical model simulations. A series of experiments are conducted for a range of mechanical excitation levels and nonlinear coefficients.

2. Nonlinear synthetic impedance circuit

Synthetic impedance [24–26] is a type of voltage-controlled current source (VCCS) that emulates an arbitrary two-terminal circuit element. The relationship between current output and voltage input is implemented using a digital controller, which enables the creation of arbitrary linear/nonlinear and static/time-varying circuit components. In this work, synthetic impedance is implemented using a Howland current pump (HCP) and an National Instruments CompactRIO controller operating at 200 kHz. The circuit diagram is shown in figure 1.

The relationship between the input voltage (i.e. the piezoelectric voltage) and the supplied current $i(t)$ is given by

$$i(t) = \frac{v_o(t)}{R_c} = \frac{\mathcal{H}\{v_p(t)\}}{R_c} \tag{1}$$

where R_c is a reference resistance in the circuit and $v_o(t) = \mathcal{H}\{v_p(t)\}$ is the output voltage from the controller, calculated as a nonlinear integro-differential operator $\mathcal{H}$ acting on the measured piezoelectric voltage $v_p(t)$. By varying the behavior of the digital controller, the form of the operator $\mathcal{H}$ can be varied, thus enabling the creation of arbitrary circuit nonlinearities of the form $i(t) = \mathcal{Y}\{v_p(t)\}$, where $\mathcal{Y} = \mathcal{H}/R_c$ is a nonlinear circuit admittance. For the purpose of this work, the circuit operator $\mathcal{H}$ is assumed to take the form

$$\mathcal{H}\{v_p(t)\} = K_p v_p(t) + K_i \int_0^t v_p(\tau)d\tau + K_c \left(\int_0^t v_p(\tau)d\tau\right)^3 \tag{2}$$

where K_p, K_i, and K_c are the proportional, integral, and integral-cubic gains respectively. This form of $\mathcal{H}$ realizes the

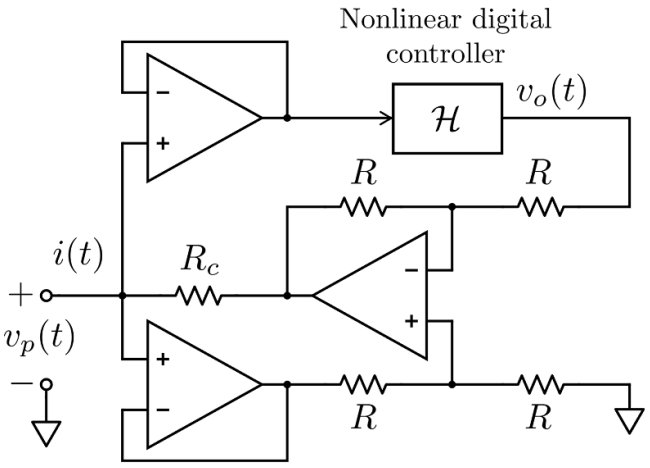

Figure 1. HCP-based synthetic impedance circuit with a nonlinear controller with operator $\mathcal{H}$.

parallel connection of a resistor, inductor, and nonlinear cubic inductor. To realize this behavior experimentally, the integrals are approximated on the digital controller using the trapezoidal rule. The gains K_p, K_i, and K_c can be smoothly varied using a LabVIEW interface that interfaces with the Field Programmable Gate Array, such that both the linear and nonlinear behavior of the circuit can be externally tuned.

3. Modeling and analysis of the electromechanical system

3.1. Modeling assumptions and structural parameters

The coupled electromechanical system being modeled consists of a clamped-free bimorph cantilevered beam (with symmetric laminates) under harmonic base excitation shunted to a synthetic impedance circuit which emulate linear and nonlinear electrical components. The piezoelectric layers, attached to each side of the substructure layer, are connected in series with opposite poling directions along the thickness of the piezoelectric layers to facilitate the experimental setup. Figures 2(a), (b) and (c), respectively, illustrate the configuration of the cantilever shunted respectively to a linear resistor, a linear resistor and a linear inductor connected in parallel, and finally a linear resistor, a linear inductor and a nonlinear inductor connected in parallel.

Table 1 lists the geometric and material properties of for the brass-reinforced thin piezoelectric bimorph cantilever used in the experiments. Since the length to total thickness ratio of the beam is high (more than 80) and since the focus will be placed on the first bending mode, the Euler-Bernoulli beam theory is justified, in which rotary inertia and shear deformation are neglected. The base of the beam undergoes harmonic displacement in the transverse direction of the beam. It is also assumed that the system exhibits low excitation levels in order to keep the material nonlinearities [6] negligible. Furthermore, the beam is stiff and/or the excitation levels are also low enough so the geometric hardening and inertial softening effects [7] of the cantilever are not pronounced. The individual piezoelectric and substructure materials are assumed to be uniform and homogeneous. The electrodes on each side of the piezoelectric layers are assumed to be negligibly thin (and are perfectly conductive) so that their thicknesses can be disregarded in the model.

3.2. Review of the linear electromechanical system

A brief review of the linear distributed-parameter electromechanical system is given first. The governing linearized equations of motion of the bimorph cantilever beam (shunted to a linear electrical circuit) under harmonic base excitation [28, 29] are

$$EI\frac{\partial^4 w_{rel}(x,t)}{\partial x^4} + c_{sp}\frac{\partial^5 w_{rel}(x,t)}{\partial x^4 \partial t} + c_{mp}\frac{\partial w_{rel}(x,t)}{\partial t} + m\frac{\partial^2 w_{rel}(x,t)}{\partial t^2} - \vartheta v_p(t)\left(\frac{\mathrm{d}\delta(x)}{\mathrm{d}x} - \frac{\mathrm{d}\delta(x-l)}{\mathrm{d}x}\right) = -m\frac{\mathrm{d}^2 w_b(t)}{\mathrm{d}t^2} \tag{3}$$

$$C_p\frac{\mathrm{d}v_p(t)}{\mathrm{d}t} + Yv_p(t) + \vartheta\int_0^l \frac{\partial^3 w_{rel}(x,t)}{\partial x^2 \partial t}dx = 0 \tag{4}$$

where $w_{rel}(x,t)$ is the transverse displacement of the beam at position x and time t, relative to the transverse base displacement $w_b(t)$; $v_p(t)$ is the voltage across the shunt (i.e. across the electrode leads), c_{sp} and c_{mp} are the stiffness-proportional (strain-rate) and mass-proportional (viscous air) damping coefficients, respectively; ϑ is the electromechanical coupling term, δ is the Dirac delta function, and Y is the external shunt admittance across the electrode pair. The expressions for the bending stifness, EI, of the beam cross-section for the short circuit condition, the mass per unit length, m, the electromechanical coupling term, ϑ, and the equivalent inherent capacitance of the two piezoelectric layers connected in series, C_p, can be found in [28, 29] for plane-stress conditions.

One can express the vibration response relative to the moving base as a modal expansion in terms of the undamped short-circuit rth mode shape (mass-normalized eigenfunction), $\phi_r(x)$, and the rth modal coordinate, $\eta_r(t)$:

$$w_{rel}(x,t) = \sum_{r=1}^{\infty}\phi_r(x)\eta_r(t), \tag{5}$$

where

$$\phi_r(x) = \sqrt{\frac{1}{ml}}\left[\cos\frac{\lambda_r}{l}x - \cosh\frac{\lambda_r}{l}x + \frac{\sin\lambda_r - \sinh\lambda_r}{\cos\lambda_r + \cosh\lambda_r} \times \left(\sin\frac{\lambda_r}{l}x - \sinh\frac{\lambda_r}{l}x\right)\right]. \tag{6}$$

Here, the eigenvalue of the rth mode of the system, λ_r is obtained from the characteristic equation given by

$$1 + \cos\lambda\cosh\lambda = 0. \tag{7}$$

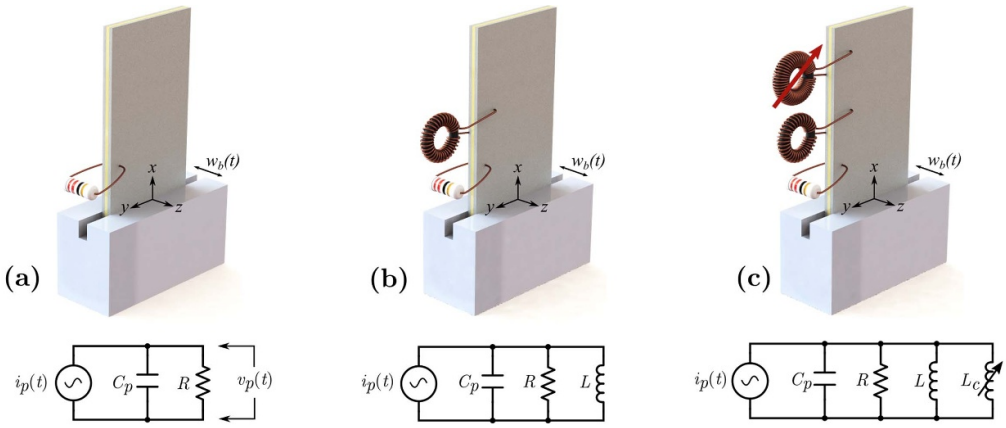

Figure 2. Bimorph piezoelectric cantilever shunted to the emulated electrical components: (a) linear resistor; (b) linear resistor and linear inductor connected in parallel; (c) linear resistor, linear inductor and nonlinear cubic inductor connected in parallel. The beam is clamped at its base and free at the other end. $w_b(t)$ is the displacement of the base of the beam as a function of time. The piezoelectric part is represented by a current source $i_p(t)$ in parallel to an equivalent capacitor C_p.

Table 1. Material and geometric properties of the bimorph piezoelectric cantilever used in the experiments.

Parameter	Definition	Value
ρ_p	Mass density of the piezoelectric layer	7800 kg m^{-3}
ρ_s	Mass density of the substructure layer	8500 kg m^{-3}
$\bar{c}_{11}^E$	Elastic modulus of the piezoelectric layer at constant electric field	66 GPa
c_s	Elastic modulus of the substructure layer	100 GPa
$\bar{e}_{31}$	Piezoelectric stress constant	-12.3 C m^{-2}
$\bar{\varepsilon}_{33}^S$	Dielectric permittivity at constant strain	14.8 nF m^{-1}
C_p	Equivalent capacitance of the two piezoelectric layers	52 nF
l	Length of the beam	57.9 mm
b	Width of the beam	31.75 mm
h_p	Thickness of each piezoelectric layer	0.267 mm
h_s	Thickness of the substructure layer	0.127 mm

Substituting the modal expansion equation (5) into the governing equations (3) and (4) and applying orthogonality conditions, one can obtain the modal electromechanical equations as

$$\frac{\mathrm{d}^2\eta_r(t)}{\mathrm{d}t^2} + 2\zeta_r\omega_r\frac{\mathrm{d}\eta_r(t)}{\mathrm{d}t} + \omega_r^2\eta_r(t) - \theta_r v_p(t) = f_r(t) \tag{8}$$

$$C_p\frac{\mathrm{d}v_p(t)}{\mathrm{d}t} + Yv_p(t) + \sum_{r=1}^{\infty}\theta_r\frac{\mathrm{d}\eta_r(t)}{\mathrm{d}t} = 0 \tag{9}$$

where ζ_r is the modal damping ratio (which can be expressed in terms of stiffness-proportional and mass-proportional damping coefficients [29]), ω_r is the rth undamped natural frequency of the beam in short-circuit condition obtained from

$$\omega_r = \lambda_r^2\sqrt{\frac{EI}{ml^4}}. \tag{10}$$

The modal forcing due to an arbitrary base motion, $f_r(t)$, and the modal electromechanical coupling term, θ_r, are respectively given by

$$f_r(t) = -m\frac{\mathrm{d}^2w_b(t)}{\mathrm{d}t^2}\int_0^l \phi_r(x)\mathrm{d}x \tag{11}$$

$$\theta_r = \bar{e}_{31}bh_{pc}\left.\frac{\mathrm{d}\phi_r(x)}{\mathrm{d}x}\right|_{x=l} \tag{12}$$

where h_{pc} is the distance from the neutral axis to the center of the piezoelectric layer (in thickness direction), b is the width of the piezoelectric layer, and $\bar{e}_{31}$ is the piezoelectric constant (table 1).

For harmonic base excitation of the form $W_b(t) = W_0\mathrm{e}^{j\omega t}$, the voltage and the vibration FRFs, per base acceleration are

$$\frac{v_p(t)}{-\omega^2 W_0\mathrm{e}^{j\omega t}} = \frac{\sum_{r=1}^{\infty}\frac{-j\omega\theta_r\sigma_r}{\omega_r^2-\omega^2+j2\zeta_r\omega_r\omega}}{Y + j\omega C_p^{eq} + \sum_{r=1}^{\infty}\frac{j\omega\theta_r^2}{\omega_r^2-\omega^2+j2\zeta_r\omega_r\omega}} \tag{13}$$

$$\frac{w_{rel}(l,t)}{-\omega^2 W_0\mathrm{e}^{j\omega t}} = \sum_{r=1}^{\infty}\left[\left(\sigma_r - \theta_r\frac{\sum_{r=1}^{\infty}\frac{j\omega\theta_r\sigma_r}{\omega_r^2-\omega^2+j2\zeta_r\omega_r\omega}}{Y + j\omega C_p^{eq} + \sum_{r=1}^{\infty}\frac{j\omega\theta_r^2}{\omega_r^2-\omega^2+j2\zeta_r\omega_r\omega}}\right) \times \frac{\phi_r(l)}{\omega_r^2 - \omega^2 + j2\zeta_r\omega_r\omega}\right] \tag{14}$$

where

$$\sigma_r = -m\int_0^l \phi_r(x)dx. \tag{15}$$

Note that the emulated circuit admittance Y is a linear admittance here, e.g. resistive or resistive-inductive as in figures 2(a) and (b). The summation signs can be dropped when the focus is placed on the first vibration mode ($r = 1$ only) which will be the case in the experiments of this work.

3.3. Nonlinear system and its electromechanical modeling

In the synthetic impedance (VCCS), substituting (2) into (1), the current supplied by the synthetic impedance circuit becomes

$$i(t) = \frac{K_p}{R_c}v_p(t) + \frac{K_i}{R_c}\int_0^t v_p(\tau)d\tau + \frac{K_c}{R_c}\left(\int_0^t v_p(\tau)d\tau\right)^3. \tag{16}$$

The governing electromechanical equations for the cantilevered piezoelectric structure for vibrations around the first bending mode become

$$\frac{\mathrm{d}^2 w_{rel}(l,t)}{\mathrm{d}t^2} + 2\zeta_1\omega_1\frac{\mathrm{d}w_{rel}(l,t)}{\mathrm{d}t} + \omega_1^2 w_{rel}(l,t) - \phi_1(l)\theta_1 v_p(t) = \phi_1(l)f_1(t) \tag{17}$$

$$C_p\frac{\mathrm{d}v_p(t)}{\mathrm{d}t} + \frac{\theta_1}{\phi_1(l)}\frac{\mathrm{d}w_{rel}(l,t)}{\mathrm{d}t} + \frac{1}{R_b}v_p(t) + \frac{K_p}{R_c}v_p(t) + \frac{K_i}{R_c}\int_0^t v_p(\tau)\mathrm{d}\tau + \frac{Kc}{R_c}\left(\int_0^t v_p(\tau)\mathrm{d}\tau\right)^3 = 0 \tag{18}$$

where ω_1 is the fundamental undamped natural frequency of the beam in short-circuit conditions; ζ_1, θ_1, $\phi_1(l)$ and $f_1(t)$ are the the first bending mode's damping ratio, the modal electromechanical coupling term, the eigenfunction evaluated at the tip of the beam, and the modal forcing due to base excitation, respectively, and R_b is the bias resistance used to dissipate DC bias current from the op-amp inputs. One can rewrite the governing equations in terms of the emulated electrical components, namely the linear resistor, R, the linear inductor, L, and the nonlinear cubic inductor, L_c:

$$\frac{\mathrm{d}^2 w_{rel}(l,t)}{\mathrm{d}t^2} + 2\zeta_1\omega_1\frac{\mathrm{d}w_{rel}(l,t)}{\mathrm{d}t} + \omega_1^2 w_{rel}(l,t) - \phi_1(l)\theta_1 v_p(t) = \phi_1(l)f_1(t) \tag{19}$$

$$C_p\frac{\mathrm{d}v_p(t)}{\mathrm{d}t} + \frac{\theta_1}{\phi_1(l)}\frac{\mathrm{d}w_{rel}(l,t)}{\mathrm{d}t} + \frac{1}{R}v_p(t) + \frac{1}{L}\int_0^t v_p(\tau)d\tau + \frac{1}{L_c}\left(\int_0^t v_p(\tau)d\tau\right)^3 = 0 \tag{20}$$

where the emulated electrical components are

$$R = \frac{R_c R_b}{K_p R_b + R_c}, \qquad L = \frac{R_c}{K_i}, \qquad L_c = \frac{R_c}{K_c}. \tag{21}$$

We will directly explore strongly nonlinear scenarios (with the jump phenomenon etc) and employ time-domain numerical solution to solve the governing nonlinear differential equations. To this end, we cast the governing equations into first-order form by using the following state variables:

$$x_1 = w_{rel}(l,t), \qquad x_2 = \frac{\mathrm{d}w_{rel}(l,t)}{\mathrm{d}t},$$
$$x_3 = \int_0^t v_p(\tau)d\tau, \qquad x_4 = v_p(t), \tag{22}$$

yielding

$$\begin{aligned}
\dot{x}_1 &= x_2\\
\dot{x}_2 &= -\omega_1^2 x_1 - 2\zeta_1\omega_1 x_2 + \phi_1(l)\theta_1 x_4 + \phi_1(l)f_1(t)\\
\dot{x}_3 &= x_4\\
\dot{x}_4 &= -\frac{\theta_1}{\phi_1(l)C_p}x_2 - \frac{1}{LC_p}x_3 - \frac{1}{RC_p}x_4 - \frac{1}{L_cC_p}x_3^3.
\end{aligned} \tag{23}$$

Then, the Runge–Kutta method (ode45 in MATLAB) is used to solve the state variables at steady state for a range of excitation frequencies. The root mean square (RMS) values of the responses are obtained for plotting the frequency response curves to compare with the experiments.

3.4. Representative analytical and numerical simulations of the system response

To ensure the accuracy of the numerical model in predicting the FRFs of the bimorph cantilever under harmonic base excitation, time-domain numerical simulation results are compared with the analytical ones for the resistive shunt and the resistive-inductive shunt scenarios (figures 2(a) and (b), respectively). Linear voltage and transmissibility FRFs for the resistive shunt and the resistive-inductive shunt cases are shown in figures 3 and 4, respectively, with a select resistor case for time-domain numerical simulation. The results show excellent agreement between the numerical and the analytical models.

A set of nonlinear simulations are performed next. In order to observe the effect of base acceleration amplitude on the frequency response of the nonlinear system with cubic inductance (figure 2(c)), we numerically simulate the system response considering continuous range of base acceleration levels for an arbitrarily selected nonlinear coefficient, $K_c = 3\times10^6\,\Omega\,\mathrm{H}^{-3}$. Figure 5 depicts heatmaps of the voltage and transmissibility FRFs of the nonlinear system with up-sweep and down-sweep scenarios. Both linear and nonlinear results are experimentally validated in the next section.

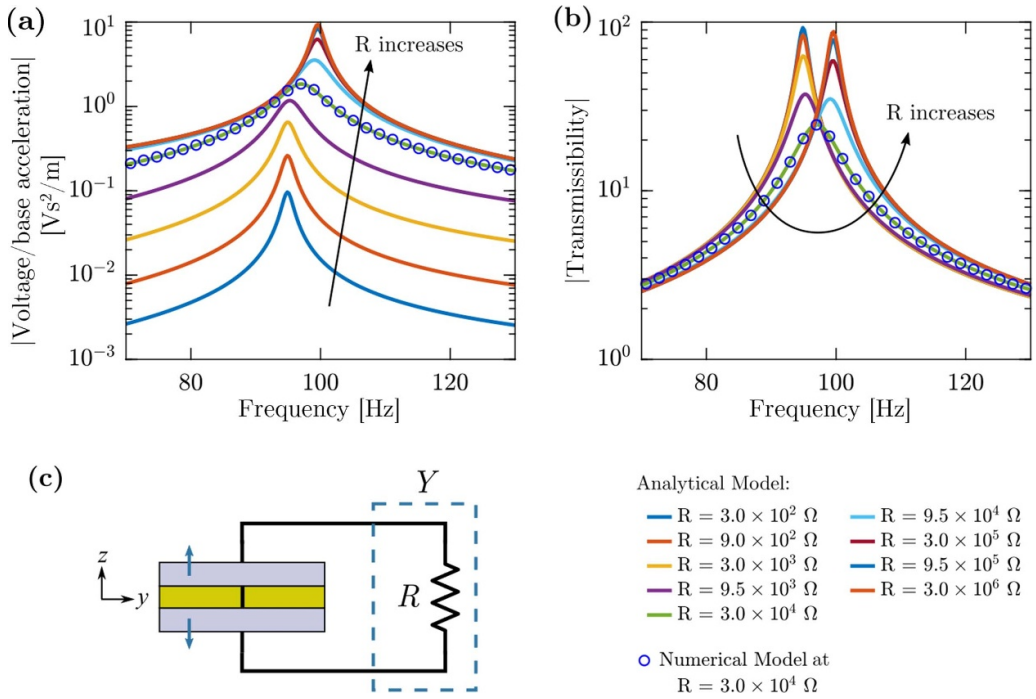

Figure 3. (a) Voltage and (b) transmissibility FRFs (in magnitude form) of the bimorph cantilever shunted to a linear resistive circuit (analytical simulations and time-domain numerical simulations for a select resistive load); (c) schematic of the shunted bimorph for this case.

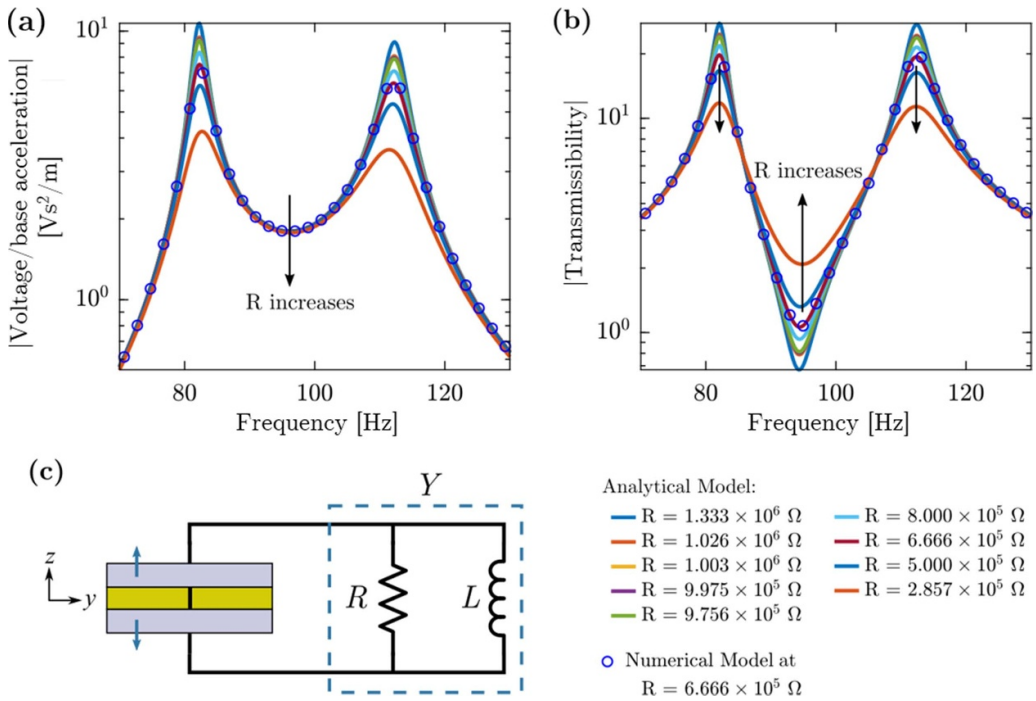

Figure 4. (a) Voltage and (b) transmissibility FRFs (in magnitude form) of the bimorph cantilever shunted to a linear resistive-inductive circuit (analytical simulations and time-domain numerical simulations for a select resistive load); (c) schematic of the shunted bimorph for this case.

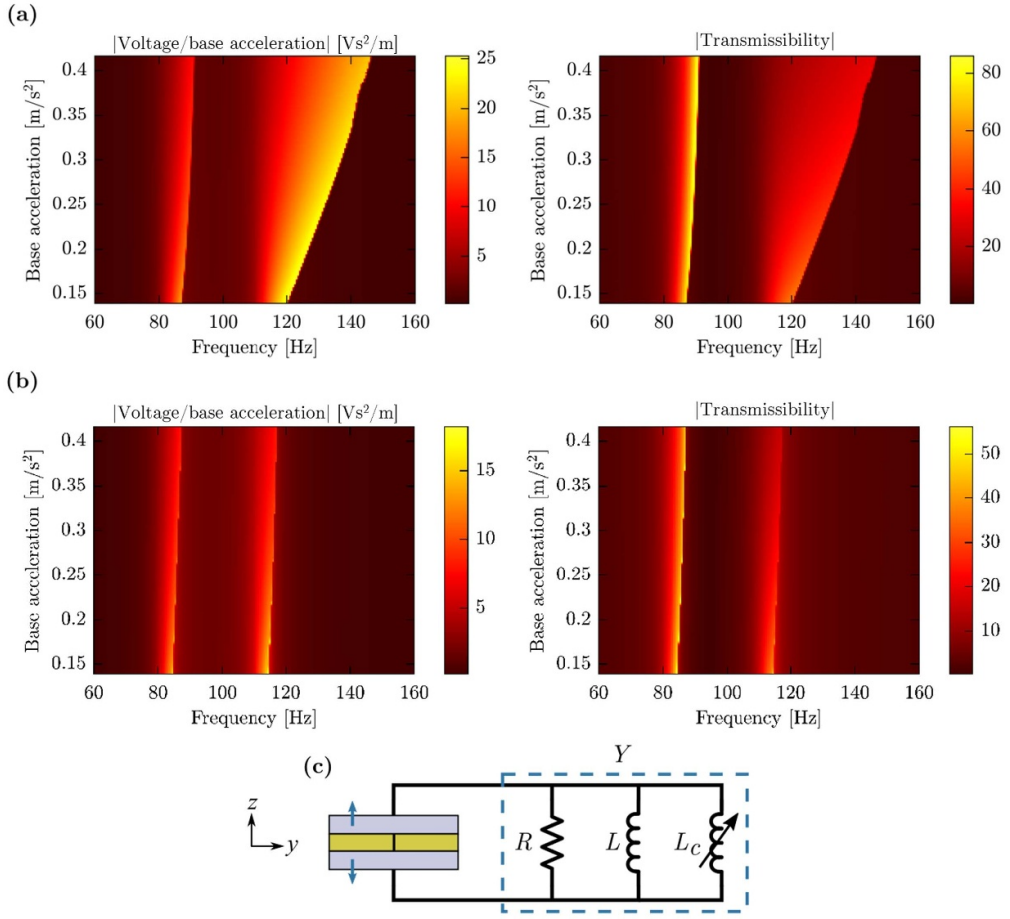

Figure 5. (a) Up-sweep and (b) down-sweep numerical simulations of the voltage and transmissibility frequency response curves (magnitude form) of the bimorph cantilever shunted to a nonlinear circuit comprising a linear resistor, linear inductor, and nonlinear positive cubic inductor for a range of base acceleration levels; (c) schematic of the shunted bimorph for this case.

4. Experimental demonstration and model validation

4.1. Experimental procedure

In order to demonstrate the nonlinear synthetic inductance and to validate the numerical model, a series of experiments are conducted. First, linear transmissibility and voltage FRFs are obtained for the emulated linear synthetic shunt cases, with the bimorph cantilever beam connected to a linear resistive shunt then to a linear resistive-inductive shunt, as depicted in figures 2(a) and (b), respectively, and linear model parameter identification (e.g. damping) and model updating are performed. In both cases, namely *R* and *RL* shunt circuits, the resistance value is swept from short-circuit to open-circuit conditions. The linear parameters are then applied to the nonlinear numerical model along with the nonlinear coefficient to demonstrate the nonlinear shunt and to evaluate the fidelity of the nonlinear model in predicting the nonlinear system dynamics. The nonlinear shunt, as previously mentioned, comprises a linear resistor, a linear inductor, and a nonlinear cubic inductor connected in parallel as shown in figure 2(c).

In order to capture the jump phenomenon expected from the saddle-node bifurcations of the Duffing nonlinearity, the experiments are performed as up and down frequency sweeps with a low rate of 3 Hz min^{-1}. Since the response of the beam in the nonlinear system depends on the base excitation amplitude, the experiments are conducted at various RMS values of the base acceleration amplitude (15, 20, 25 and 30 m*g*, where *g* is the gravitational acceleration), with a constant base acceleration at each sweep. Up and down sweeps are performed from 60 to 160 Hz at each base excitation level to capture the first bending mode of the beam. The selected parameters in the nonlinear synthetic impedance circuits are shown in table 2. Note that the integral-cubic gain is varied as the nonlinear coefficient and the same base acceleration levels are tested for each case.

Table 2. Electrical circuit parameters in the synthetic impedance circuit.

Parameter	Definition	Value
R_c	Reference resistance	$1 \times 10^4\,(\Omega)$
R_b	Bias resistance	$1 \times 10^6\,(\Omega)$
K_p	Proportional gain	-0.015
K_i	Integral gain	$185\,(\Omega\,\mathrm{H}^{-1})$ or (Hz)
K_c	Integral-cubic gain	$1 \times 10^6 \rightarrow 5 \times 10^6\,(\Omega\,\mathrm{H}^{-3})$

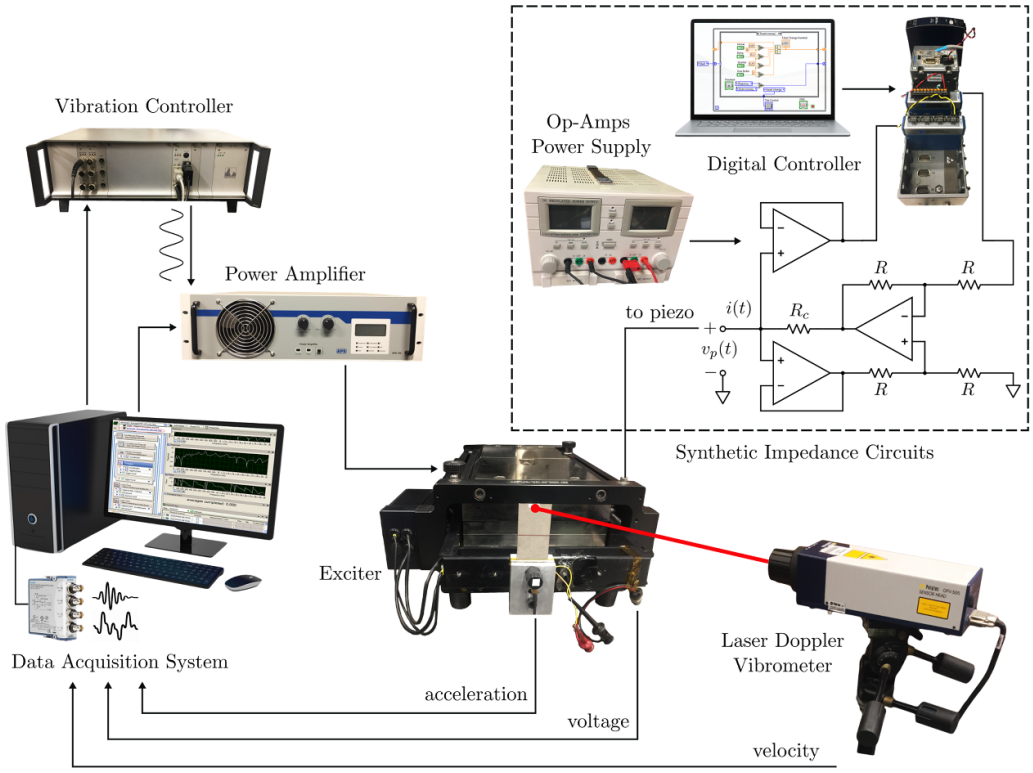

Figure 6. An overview of the experimental setup showing the bimorph piezoelectric cantilever under base excitation shunted to synthetic impedance circuit and various equipment employed in excitation and measurement.

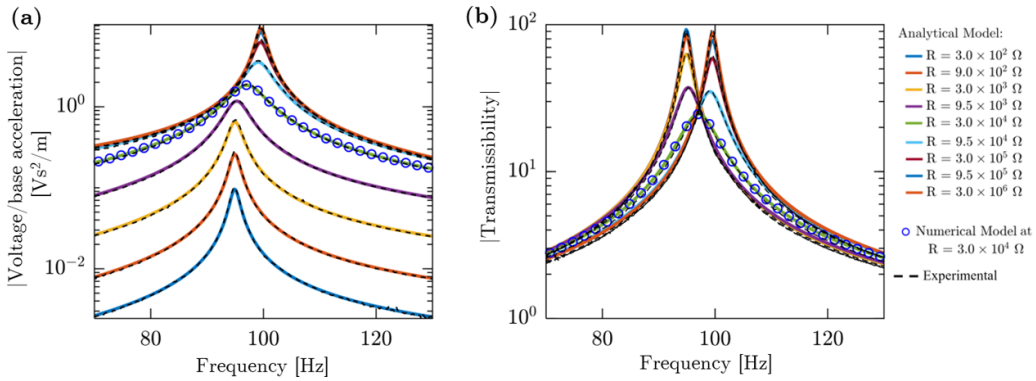

Figure 7. (a) Voltage and (b) transmissibility FRFs (in magnitude form) of the bimorph beam shunted to a resistor. Experimental results are plotted in dashed black lines while colored lines represent analytical solution. Numerical prediction is shown in blue markers.

4.2. Experimental setup

An overview of the experimental setup is displayed in figure 6. The beam is clamped vertically to the armature of an APS-400 electrodynamic exciter, which is driven by an APS 145 power amplifier. The base acceleration is measured by a C114973 Kistler accelerometer that is connected to Kistler power supply, while the beam tip transverse velocity is measured using a Polytec OFV-505 laser Doppler vibrometer (LDV). The LDV is controlled by a Polytec OFV-5000 vibrometer controller. The voltage across the piezoelectric electrodes is measured directly from the beam. The data is acquired using a National Instruments Module 4431-2. In the linear FRF extraction experiments, low-intensity white noise is used as the input to the shaker to avoid any nonlinearity. In the nonlinear experiments, the shaker is controlled by a SPEKTRA VCS-201 vibration controller, which uses feedback from the base accelerometer to maintain a constant acceleration level during up and down sweeps at the mentioned slow rate.

4.3. Results and discussion

In the experiments, linear shunt circuit elements are emulated first. The voltage to base acceleration and transmissibility FRFs of the beam shunted to a linear resistor are shown in figure 7. The FRFs illustrate the effect of changing the resistance load from the short circuit ($R \to 0$) to the open circuit ($R \to \infty$), passing through the optimal resistance

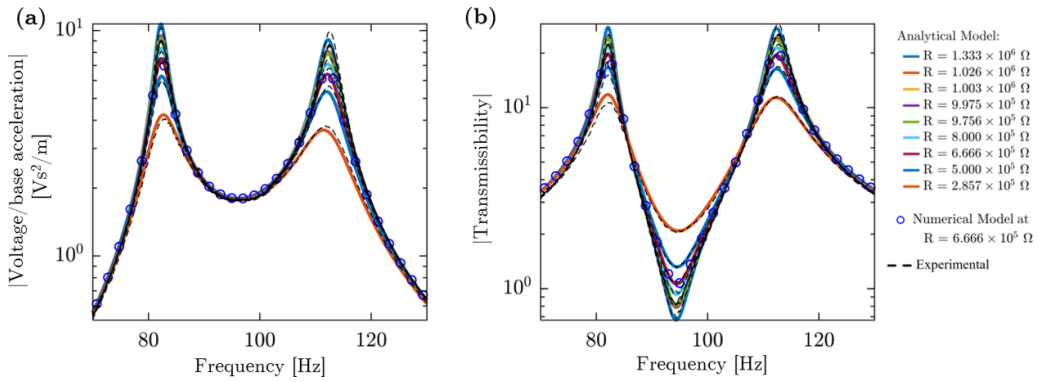

Figure 8. (a) Voltage and (b) transmissibility FRFs (in magnitude form) of the bimorph beam shunted to a resistor and inductor connected in parallel. Experimental results are plotted in dashed black lines while colored lines represent analytical solution. Numerical prediction is shown in blue markers.

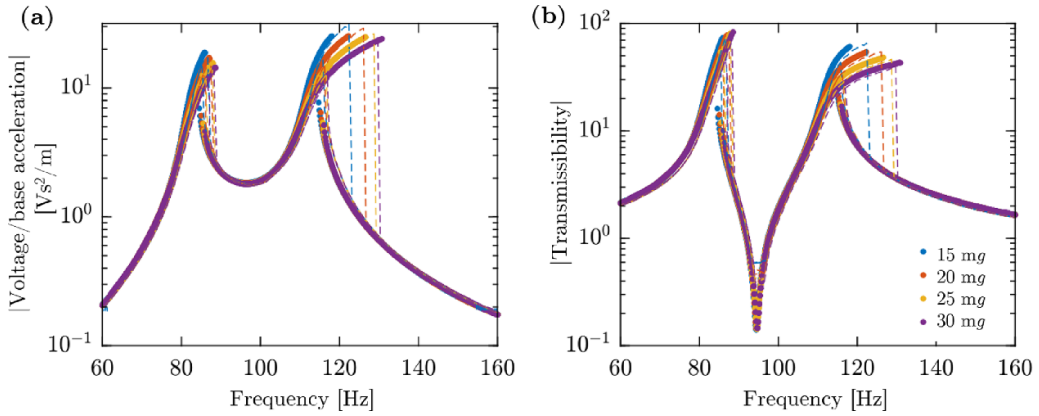

Figure 9. (a) Voltage and (b) transmissibility frequency response curves (in magnitude form) of the bimorph beam shunted to the nonlinear circuit with nonlinear cubic coefficient $K_c = 1 \times 10^6\,\Omega\,\mathrm{H}^{-3}$. Experimental results are plotted in dashed lines while markers represent numerical predictions.

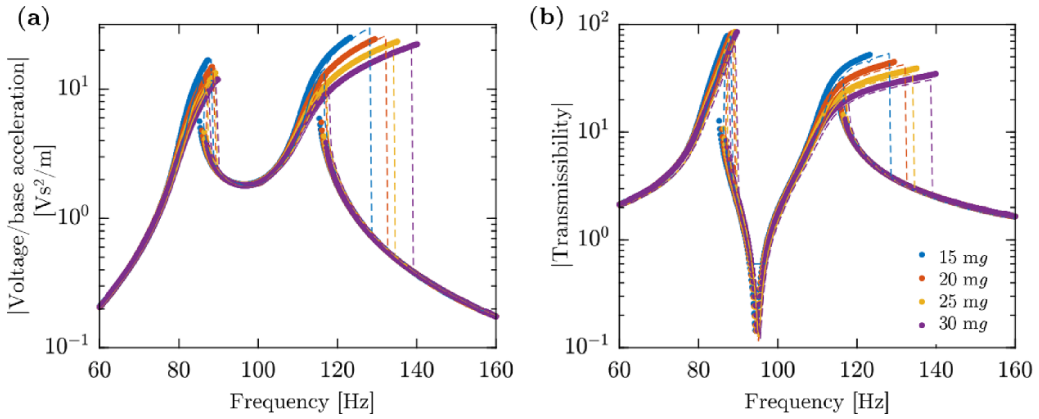

Figure 10. (a) Voltage and (b) transmissibility frequency response curves (in magnitude form) of the bimorph beam shunted to the nonlinear circuit with nonlinear cubic coefficient $K_c = 2 \times 10^6\,\Omega\,\mathrm{H}^{-3}$. Experimental results are plotted in dashed lines while markers represent numerical predictions.

near $R = 30\,\mathrm{k}\Omega$. Similarly, the FRFs are obtained for linear resistive-inductive shunt damping for a range of resistive loads to confirm the standard linear synthetic circuit dynamics as shown in figure 8. Overall, both figures 7 and 8 show excellent agreement between the analytical, numerical (i.e. time-domain), and experimental results, validating the linear electromechanical model parameters for the system.

Nonlinear experiments are then conducted for a set of cubic nonlinear coefficients and base acceleration levels. The nonlinear voltage and transmissibility frequency response curves are shown in figures 9–13, for the hardening cubic nonlinear

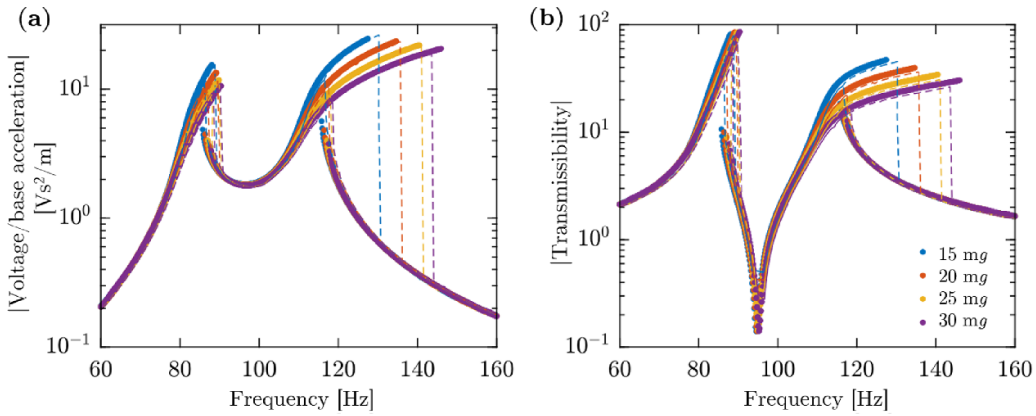

Figure 11. (a) Voltage and (b) transmissibility frequency response curves (in magnitude form) of the bimorph beam shunted to the nonlinear circuit with nonlinear cubic coefficient $K_c = 3 \times 10^6\,\Omega\,\mathrm{H}^{-3}$. Experimental results are plotted in dashed lines while markers represent numerical predictions.

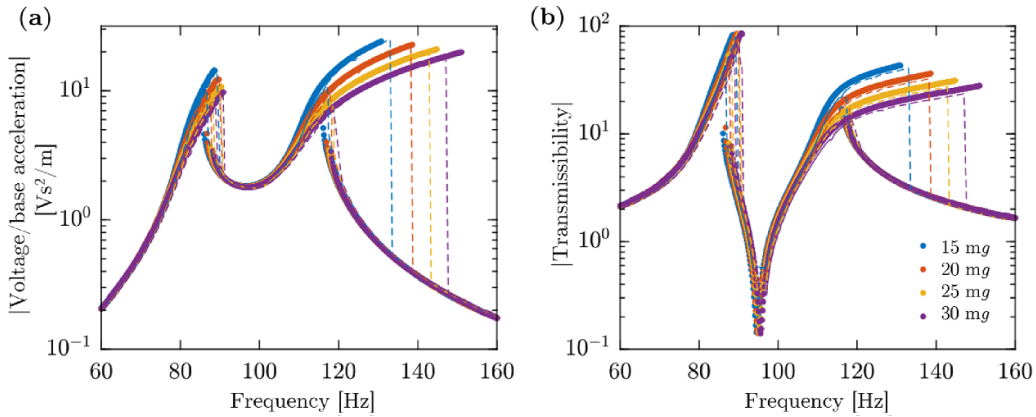

Figure 12. (a) Voltage and (b) transmissibility frequency response curves (in magnitude form) of the bimorph beam shunted to the nonlinear circuit with nonlinear cubic coefficient $K_c = 4 \times 10^6\,\Omega\,\mathrm{H}^{-3}$. Experimental results are plotted in dashed lines while markers represent numerical predictions.

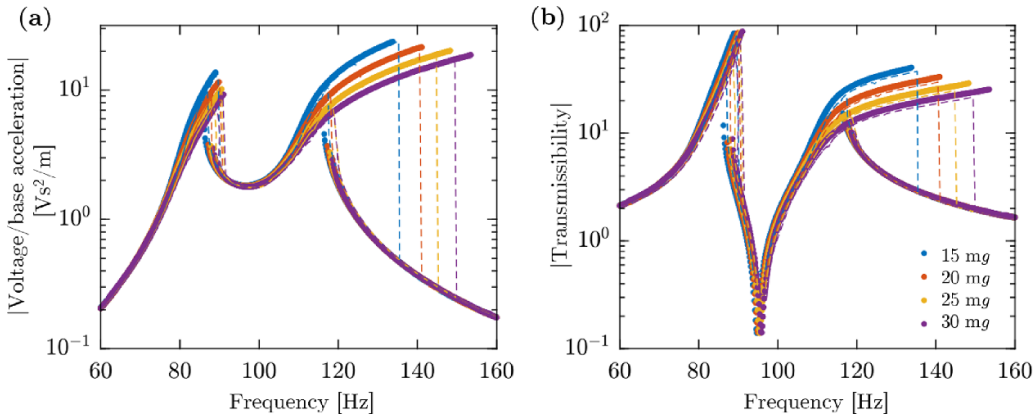

Figure 13. (a) Voltage and (b) transmissibility frequency response curves (in magnitude form) of the bimorph beam shunted to the nonlinear circuit with nonlinear cubic coefficient $K_c = 5 \times 10^6\,\Omega\,\mathrm{H}^{-3}$. Experimental results are plotted in dashed lines while markers represent numerical predictions.

coefficient values $K_c = 1 \times 10^6\,\Omega\,\mathrm{H}^{-3}$, $2 \times 10^6\,\Omega\,\mathrm{H}^{-3}$, $3 \times 10^6\,\Omega\,\mathrm{H}^{-3}$, $4 \times 10^6\,\Omega\,\mathrm{H}^{-3}$, and $5 \times 10^6\,\Omega\,\mathrm{H}^{-3}$, respectively. In each case, the resonances are substantially distorted compared to the linear counterpart in figure 8. Both modes exhibit Duffing-type hardening nonlinearity, but the higher frequency resonance exhibits a significantly wider hardening bandwidth. Additionally, the introduction of cubic nonlinearity does not significantly affect the linear antiresonance, which exhibits

strong attenuation at all excitation and nonlinearity levels. As expected, the hardening bandwidth can be increased either by increasing the excitation level (i.e. base acceleration) or by increasing the nonlinear coefficient. While the primary purpose of this work is *not* to design an absorber (but to demonstrate the synthetic nonlinear inductive shunt), the high-frequency hardening branch achieves good attenuation of the original resonance without compromising the attenuation due to the antiresonance. Overall, the voltage and transmissibility frequency response curves show a good match between the numerical model (using the Runge–Kutta method) and the experimental results. The primary discrepancy lies in the prediction of the exact jump frequency, which is sensitive to the exact environmental conditions during experiments.

5. Conclusions

A digitally programmable nonlinear synthetic impedance circuit that can emulate Duffing-type hardening nonlinearity is demonstrated in this work. The electromechanical system dynamics is modeled and simulated using time-domain numerical solution with experimental validations on a bimorph cantilever beam under harmonic base excitation. This fully coupled nonlinear electromechanical system, composed of the bimorph beam shunted to a programmable nonlinear synthetic impedance circuit, is studied for different values of the nonlinear inductance coefficient and for a range of mechanical excitation levels. The typical hardening behavior of a Duffing oscillator with an enhanced frequency bandwidth is observed in the voltage and transmissibility FRFs due to the synthetic impedance-based cubic inductance. This type of circuit nonlinearity is not easily achievable using analog elements, since it would require specialized analog multiplier circuits (and would not be easily tunable in that case). Experimental measurements reveal a good match with the numerical simulations at various cubic nonlinearity coefficients and base excitation levels. The introduced nonlinearities can attenuate the high-frequency resonance introduced by the circuit without compromising the attenuation at the antiresonance. More broadly, the developed nonlinear synthetic impedance system is a powerful tool for investigating a broad range of nonlinear vibration absorbers, such as systems with high-order nonlinearities, mixed hardening and softening behaviors, or essentially nonlinear behavior. Furthermore, synthetic impedance allows the nonlinear coefficients to be varied over a wide range, enabling the introduction of strongly nonlinear vibrational response at very low excitation levels on demand.

Data availability statement

The data that support the findings of this study are available upon reasonable request from the authors.

ORCID iDs

Obaidullah Alfahmi https://orcid.org/0000-0001-9535-7384
Christopher Sugino https://orcid.org/0000-0001-7547-4874
Alper Erturk https://orcid.org/0000-0003-0110-5376

References

[1] Oueini S S, Nayfeh A H and Pratt J R 1998 A nonlinear vibration absorber for flexible structures *Nonlinear Dyn.* **15** 259–82
[2] Vakakis A F, Gendelman O V, Bergman L A, Michael McFarland D, Kerschen G and Lee Y S 2008 *Nonlinear Targeted Energy Transfer in Mechanical and Structural Systems* (Dordrecht: Springer)
[3] Ibrahim R A 2008 Recent advances in nonlinear passive vibration isolators *J. Sound Vib.* **314** 371–452
[4] Kovacic I, Brennan M J and Waters T P 2008 A study of a nonlinear vibration isolator with a quasi-zero stiffness characteristic *J. Sound Vib.* **315** 700–11
[5] Daqaq M F, Masana R, Erturk A and Dane Quinn D 2014 On the role of nonlinearities in vibratory energy harvesting: a critical review and discussion *Appl. Mech. Rev.* **66** 040801
[6] Leadenham S and Erturk A 2015 Unified nonlinear electroelastic dynamics of a bimorph piezoelectric cantilever for energy harvesting, sensing and actuation *Nonlinear Dyn.* **79** 1727–43
[7] Tan D, Yavarow P and Erturk A 2018 Resonant nonlinearities of piezoelectric macro-fiber composite cantilevers with interdigitated electrodes in energy harvesting *Nonlinear Dyn.* **92** 1935–45
[8] Yang K, Harne R L, Wang K W and Huang H 2014 Investigation of a bistable dual-stage vibration isolator under harmonic excitation *Smart Mater. Struct.* **23** 045033
[9] Romeo F, Sigalov G, Bergman L A and Vakakis A F 2015 Dynamics of a linear oscillator coupled to a bistable light attachment: numerical study *J. Comput. Nonlinear Dyn.* **10** 011007
[10] Li L and Cui P 2017 Novel design approach of a nonlinear tuned mass damper with duffing stiffness *J. Eng. Mech.* **143** 04017004
[11] Ahmadian M and Deguilio A P 2001 Recent advances in the use of piezoceramics for vibration suppression *Shock Vib. Dig.* **33** 15–22
[12] Lesieutre G A 1998 Vibration damping and control using shunted piezoelectric materials *Shock Vib. Dig.* **30** 187–95
[13] Hagood N W and von Flotow A 1991 Damping of structural vibrations with piezoelectric materials and passive electrical networks *J. Sound Vib.* **146** 243–68
[14] Clark W W 2000 Vibration control with state-switched piezoelectric materials *J. Intell. Mater. Syst. Struct.* **11** 263–71
[15] Corr L R and Clark W W 2002 Comparison of low-frequency piezoelectric switching shunt techniques for structural damping *Smart Mater. Struct.* **11** 370
[16] Richard C, Guyomar D, Audigier D and Ching G 1999 Semi-passive damping using continuous switching of a piezoelectric device *Proc. SPIE* **3672** 104–11
[17] Richard C, Guyomar D, Audigier D and Bassaler H 2000 Enhanced semi-passive damping using continuous

switching of a piezoelectric device on an inductor *Proc. SPIE* **3989** 288–99
[18] Guyomar D, Mohammadi S and Richard C 2009 Effect of boundary (support) conditions on piezoelectric damping in the case of SSDI vibration control technique *Mech. Syst. Signal Process.* **23** 501–13
[19] Lefeuvre E, Badel A, Petit L, Richard C and Guyomar D 2006 Semi-passive piezoelectric structural damping by synchronized switching on voltage sources *J. Intell. Mater. Syst. Struct.* **17** 653–60
[20] Soltani P and Kerschen G 2015 The nonlinear piezoelectric tuned vibration absorber *Smart Mater. Struct.* **24** 075015
[21] Lossouarn B, Deü J-F and Kerschen G 2017 Passive realization of a nonlinear piezoelectric tuned vibration absorber with a saturable inductor *9th European Nonlinear Dynamics Conf. (ENOC 2017)* vol 2017
[22] Zhou B, Thouverez F and Lenoir D 2014 Essentially nonlinear piezoelectric shunt circuits applied to mistuned bladed disks *J. Sound Vib.* **333** 2520–42
[23] Silva T M P, Clementino M A, De Marqui C Jr and Erturk A 2018 An experimentally validated piezoelectric nonlinear energy sink for wideband vibration attenuation *J. Sound Vib.* **437** 68–78
[24] Fleming A J, Behrens S and Moheimani S O R 2000 Synthetic impedance for implementation of piezoelectric shunt-damping circuits *Electron. Lett.* **36** 1525–6
[25] Matten G, Collet M, Cogan S and Sadoulet-Reboul E 2014 Synthetic impedance for adaptive piezoelectric metacomposite *Proc. Technol.* **15** 84–89
[26] Nečásek J, Václavík J and Márton P 2016 Digital synthetic impedance for application in vibration damping *Rev. Sci. Instrum.* **87** 024704
[27] Raze G, Jadoul A, Guichaux S, Broun V and Kerschen G 2019 A digital nonlinear piezoelectric tuned vibration absorber *Smart Mater. Struct.* **29** 015007
[28] Erturk A and Inman D J 2009 An experimentally validated bimorph cantilever model for piezoelectric energy harvesting from base excitations *Smart Mater. Struct.* **18** 025009
[29] Erturk A and Inman D J 2011 *Piezoelectric Energy Harvesting* (New York: Wiley)